Microscopy AND
Microanalysis

Original Article

Direct Observation of PFIB-Induced Clustering in Precipitation-Strengthened Al Alloys by Atom Probe Tomography

David Tweddle[1], Jonathan A. Johnson[1], M. Kapoor[2], Sean Mileski[2], John E. Carsley[2] and Gregory B. Thompson[1]*

[1]Department of Metallurgical & Materials Engineering, University of Alabama, Tuscaloosa, AL 35405, USA and [2]Novelis Global Research & Technology Center, 1950 Vaughn Road, Kennesaw, GA 30144, USA

Abstract

The effect of sample preparation on a pre-aged Al–Mg–Si–Cu alloy has been evaluated using atom probe tomography. Three methods of preparation were investigated: electropolishing (control), Ga^+ focused ion beam (FIB) milling, and Xe^+ plasma FIB (PFIB) milling. Ga^+-based FIB preparation was shown to introduce significant amount of Ga contamination throughout the reconstructed sample (≈ 1.3 at %), while no Xe contamination was detected in the PFIB-prepared sample. Nevertheless, a significantly higher cluster density was observed in the Xe^+ PFIB-prepared sample ($\approx 25.0 \times 10^{23}$ m^{-3}) as compared to the traditionally produced electropolished sample ($\approx 3.2 \times 10^{23}$ m^{-3}) and the Ga^+ FIB sample ($\approx 5.6 \times 10^{23}$ m^{-3}). Hence, the absence of the ion milling species does not necessarily mean an absence of specimen preparation defects. Specifically, the FIB and PFIB-prepared samples had more Si-rich clusters as compared to electropolished samples, which is indicative of vacancy stabilization via solute clustering.

Key words: aluminum alloys, atom probe tomography, FIB, plasma FIB, sample preparation

Introduction

Heat-treatable Al alloys, and other light metals such as Mg, are susceptible to room-temperature aging. As these alloy microstructures evolve, these changes detrimentally impact subsequent processing such as joining, forming, and even aging kinetics resulting in a "shelf-life" to the alloy. The clustering of solute atoms, which control these performance criteria, is strongly dependent on the vacancy super-saturation (Aruga et al., 2015; Poznak et al., 2018). These solute clusters, particularly in the early stages of aging, are often difficult, if not impossible, to be resolved using transmission electron microscopy (TEM) because of their size and coherent structure within the matrix. In contrast to TEM, atom probe tomography (APT), a field ion microscopy method, can resolve as well as quantify the distribution characteristics of such clusters in these early stages. APT has equal sensitivity for all elements with an analytical sensitivity of approximately 5 atomic ppm and can reconstruct the spatial location of each atom with near-perfect lattice rectification (Marquis & Hyde, 2010; Larson et al., 2013; Stephenson et al., 2013). Consequently, these attributes make this technique well suited to reveal the early stages of clustering in light metal alloys during aging at room and elevated temperatures (Buha et al., 2007; Aruga

et al., 2015; Marceau, 2016; Buchanan et al., 2017; Hu et al., 2020; Lee et al., 2021).

APT requires an ultra-sharp needle-shaped specimen ($r < 50$ nm) to enhance the electric field at the tip required for field evaporation of the surface atoms. Historically, APT specimens were shaped using electropolishing which produces specimens that are essentially "damage-free." In the past 20 years, the use of a Ga^+ focused ion beam (FIB) has become ubiquitous for APT preparation as it enables site-specific preparation of APT samples (Larson et al., 1999). While inordinately beneficial to preparation, the Ga^+ FIB does create unintended artifacts during sample preparation including amorphization of the surface (Miller et al., 2007), creation of vacancies and other point defects from "knock-on" collisions within the alloy (Idrissi et al., 2011), and embrittlement of the grain boundaries in Al alloys (Unocic et al., 2010). The impact of such defects modifies precipitation transformation pathways and accelerates aging kinetics in Al alloys (Wang et al., 2017).

Recent work by Lilensten & Gault (2020) on a commercial 6016 Al alloy has shown that cryogenic cooling during FIB lift-out and sharpening (performed at 82 K) reduces Ga^+ diffusion to the grain boundaries. While this work focused on the impact of temperature during sample preparation with a particular emphasis on Ga^+ grain boundary segregation, it did not specifically address the impact of milling created defects on solute clustering. Such knowledge is critical in elucidating the link between solute clustering and mechanical properties. Another potential strategy for light metals to mitigate ion milling damage during preparation

CrossMark

is the use of the recently introduced plasma-based FIB (PFIB) (Halpin et al., 2019; Famelton et al., 2021). This microscope employs a Xe gas to create a plasma whereupon the ions are extracted for milling. Xe is believed to mitigate prior FIB risks because it is chemically inert (Halpin et al., 2019) and has decreased penetration depth/stopping distance for the same acceleration voltage, as shown by reducing up to 40% of the amorphous damage (in Si) as compared to Ga FIBs (Kelley et al., 2013).

To date, there have been a limited number of studies that have specifically investigated the impact of point defects introduced during FIB-based sample preparation on the early stages of solute clustering behavior (Dumitraschkewitz et al., 2017; Famelton et al., 2021). As noted above, this is especially relevant for light metals where solute atoms are keenly sensitive to the disruptions in the lattice as they partition (Marceau, 2016). Recognizing the ever-increasing use of FIB milling methods to prepare APT needles, and the emerging PFIB options, this work investigates how such sample preparation, particularly the PFIB, alters the intrinsic nanostructure that ultimately influences the quantitative data that APT provides.

Methods

The Al–Mg–Si–Cu alloy, with a nominal bulk composition of Mg (0.7–1.0 wt%), Cu (0.6–0.9 wt%), Si (0.6–0.9 wt%), and remaining total minor elements (<1 wt%), was solution-treated followed by a low-temperature aging treatment at 100°C/4 h, denoted as pre-aging (PA). After PA, the case study alloy was immediately transferred to a freezer, to mitigate the impact of secondary natural aging (SNA) at room temperature (RT), and stored below −30° C till sample preparation. Additionally, a sample was electropolished following 30 days of SNA to deconvolute the impact of the sample preparation times on clustering behavior. Since electropolishing does not involve ion energy impact, but rather a gradual removal of material, these specimens are considered the control or intrinsic state of the case study alloy. The alloy in the PA condition was used as a case study for the following reasons: (1) This condition will have nucleated Mg-rich clusters. (2) There is enough solute dissolved in the matrix to capture the impact of the defects introduced during FIB sample preparation.

The electropolishing was performed using a conventional two-stage method (Yao & Zhong, 2005) with the sample cut into a rectangular geometry, denoted as a matchstick, and crimped into a Cu holding tube. In Stage 1, we utilized 10% perchloric acid in glacial acetic acid at 5 V DC until necking and separation of the matchstick occurred. In Stage 2, a mixture of 2% perchloric acid in butoxyethanol was used, again at 5 V DC, to ensure a sharp-needle-shaped specimen with a radius of <50 nm. After electropolishing, a minor contamination of Cu was observed on the tip surface (which is contributed to the electrolytic solution inadvertently contacting the copper tube holding the APT tip). Famelton et al. (2021) also noted a similar electropolishing artifact. For both works, this surface area of copper contamination was excluded from the subsequent analysis. This preparation process took approximately 4 h to complete including sectioning of the rectangular "matchstick" that was then electropolished at one end into the APT tip. Ga⁺ FIB was performed using a Tescan Lyra FIB/SEM with trenching out the region of interest at 30 kV with 1–4 nA, while sharpening was performed at 30 kV between 30–300 pA. A low-kV clean-up step was performed in the final polish at 2 kV and 120 pA to reduce ion

damage (Thompson et al., 2006). The Xe⁺ PFIB was performed using a Thermo Fisher Scientific Helios G4 PFIB CXe dual-beam FIB/SEM with initial trenching and sharpening at 30 kV and 30–3000 pA, while final polishing was performed at 2 kV and 80 pA. Effort was made to ensure the milling currents and conditions used between the two FIB instruments at each stage were as equivalent as possible. The ion milling process, regardless of instrument, took between 4 and 6 h.

APT analysis was performed on a LEAP 5000 XS in voltage mode at 35 K, with a pulse fraction of 20%, a detection rate of 0.5%, and a pulse frequency of 200 kHz. Reconstructions were performed using IVAS 3.8.4, with pole indexing and spatial distribution maps used to optimize the reconstruction parameters (Breen et al., 2015). The cluster search was performed on a region of interest away from the poles using the maximum separation method, as described by Hyde et al. (2011). To ensure consistency in the analysis of the different sample preparation methods, a value of 0.5 for the d_{max} and a N_{min} value of 17 with solute of Mg, Si, and Cu were used for each sample. In addition, the voltage range over which the data analysis was performed was between 3 kV and 5 kV. These values of d_{max} and N_{min} were selected by comparing the acquired data to a randomized dataset with the same solute concentration. Cluster searching on both datasets was then performed, with the selected values of d_{max} and N_{min} having the largest number of clearly discernible clusters compared to noise.

The number density of the clusters (N_V) was calculated as follows:

$$N_V = \frac{N\rho_{th}\eta}{N_{total}}, \qquad (1)$$

where N is the number of clusters, ρ_{th} is the theoretical density of the cluster (taken to be the same as the atomic density of Al), η is the detection efficiency of the LEAP 5000XS (80%), and N_{total} is the total number of ions in the dataset (Jenkins et al., 2020). The error of the number density is given as N_V divided by the square root of the total number of clusters.

Stopping and range of ions in matter (SRIM) modeling was performed using the SRIM 2013 software developed by Ziegler et al. (2010). Xe and Ga ions were implanted perpendicularly into a pure Al target with a depth of 100 nm and a width of 100 nm. The total implanted ion count was 50,000 ions.

Results and Discussion

Figures 1a–1c are representative APT reconstructions showing only the clusters identified, using the nearest neighbor search algorithm, in samples prepared using the three preparation methods: electropolishing (which served as the control), FIB, and PFIB. All three methods reveal qualitatively similar clustering. No Xe⁺ implantation in the PFIB sample was detected consistent with the absence of any peaks in the mass spectrum range of Xe⁺, Figure 1d. In contrast, the reconstruction of the Ga⁺ FIB sample reveals the presence of Ga, both in the mass spectrum, Figure 1e, and in the inset image in the same figure showing its concentration enrichment in the data volume. Here, the Ga accounted for ≈1.3 at% of the total collected ions. The absence of Xe⁺ could be explained by two things: (1) the lower penetration depth of Xe, as compared to Ga (Kelley et al., 2013), and (2) Xe being a gas at standard conditions and would diffuse out of the tip and be lost to the atmosphere. The lack of Xe⁺ detected in the sample,
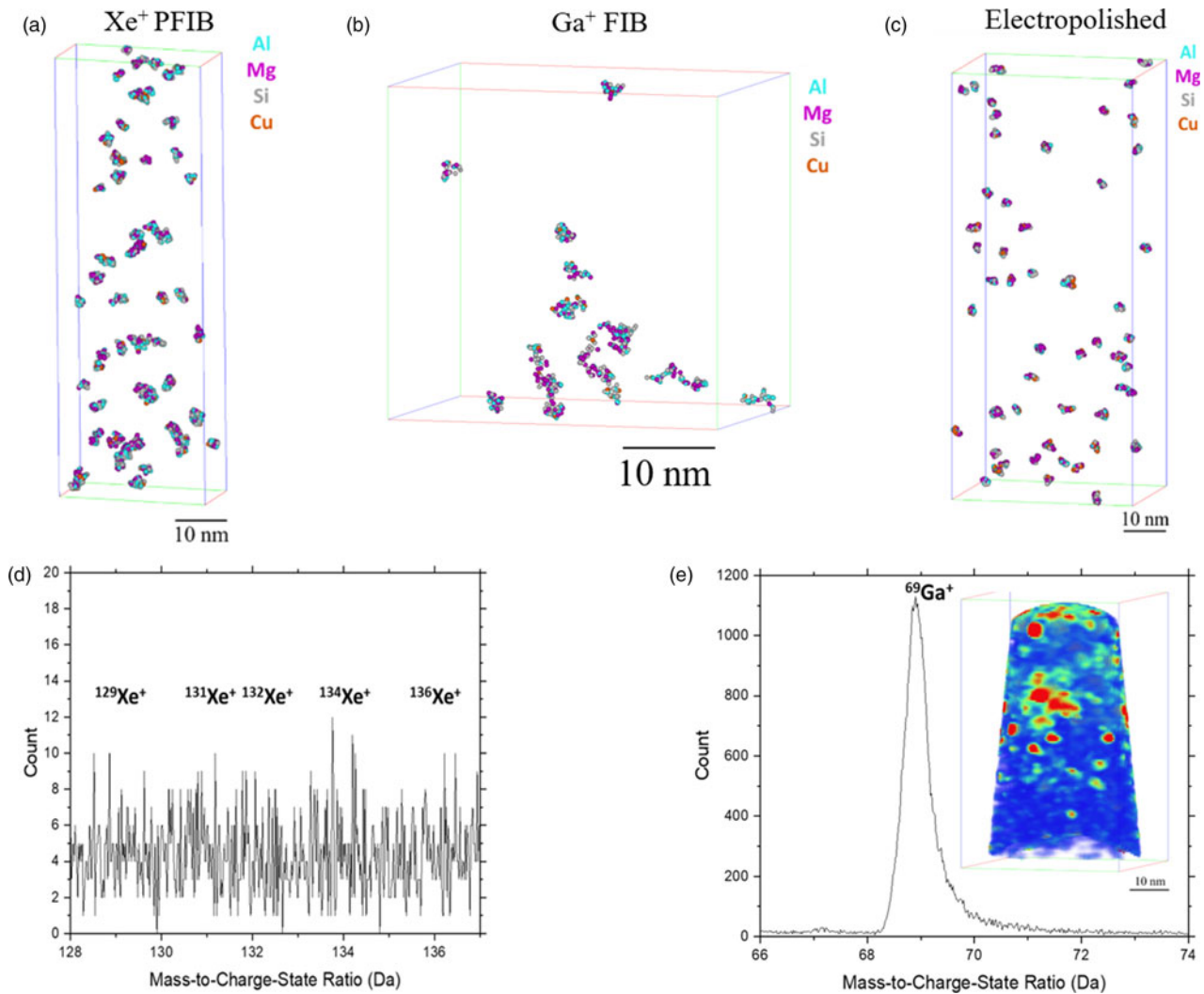
Fig. 1. Clusters detected in (**a**) a Xe⁺ PFIB sample dataset, (**b**) a Ga⁺ FIB sample dataset, and (**c**) an electropolished sample dataset. Extracts of the mass spectra from (**d**) a Xe⁺ PFIB sample dataset and (**e**) a Ga⁺ FIB sample dataset with a clear Ga⁺ peak and an inset image of the Ga concentration in the reconstruction visualized volume via density (where red indicates higher Ga concentration).

unlike Ga^+, could provide indications that this method of ion milling does not result in significant artifacts introduced into the nanostructure. In the recent work by Famelton et al. (2021), where they used a PFIB to prepare APT tips from a 6xxx alloy, they noted Xe^+ capture in their APT data volume sets, suggesting potential user-dependent variations in PFIB-prepared APT samples.

While the clusters qualitatively exist between each method, a detailed evaluation of their distribution characteristics reveals notable differences. Table 1 notes a significant modification in the number density of clusters. Specifically, Ga^+ FIB- and Xe^+ PFIB-prepared samples have approximately a doubling and nearly an order of magnitude increase in clusters for each method, respectively, as compared to the electropolished control sample. Interestingly, the cluster size is not significantly different among all the prepared samples, suggesting that the two observations from the control are not governed by kinetics. Recognizing that the number density could be influenced by differences in ambient temperature exposure from handling variations among the three preparation methods, an electropolished-prepared tip was studied from a pre-aged sample but allowed to naturally age for 30 days at ambient temperature (denoted as PA + NA/30 days). As can be seen in the tabulated results in Table 1, the number density slightly increased from $3.2 \pm 0.4 \times 10^{23}$ to $4.5 \pm 0.8 \times 10^{23}$ m⁻³ for this sample but is still lower than either the FIB or PFIB samples. This reinforces the deduction that the significant increase in cluster density is indeed a result of the specimen preparation method and not from potential (minor) handling differences between the preparation times among the three samples.

To further confirm that the sample preparation method impacts cluster formation, the cluster compositions were examined based on their Mg:Si ratio. Figure 2 is the histograms of the Mg:Si ratio where a clear demarcation between the electropolished, Ga^+ FIB, and the Xe^+ PFIB exists. Specifically, the percentage of Si-rich clusters in the electropolished samples is 33%, Table 1, whereas in the FIB and PFIB samples, the Si-rich clusters are approximately 50 and 55%, respectively. Of the two ion milling methods, the clusters in Ga^+ FIB did not reveal a clear separation based on solute enrichment, quantified via the Mg:Si ratio compared to either the electropolished sample or the PFIB sample. Collectively, the number density increases and the change in the cluster composition provide strong, quantitative

Table 1. Cluster Radius, Number Density, and the Percentage of Si-Rich of Clusters Detected in Samples Prepared via All Sample Preparation Methods.

Sample Preparation Method	Cluster Radius (nm)	Number Density (10^{23} m^{-3})	Si-Rich Clusters (Mg/Si <1)
Electropolishing	0.54 ± 0.06	3.2 ± 0.4	33%
Ga$^+$ FIB	0.58 ± 0.07	5.6 ± 1.4	50%
Xe$^+$ PFIB	0.60 ± 0.07	25.0 ± 3.0	55%
Electropolishing (30 days NA)	0.56 ± 0.06	4.5 ± 0.8	30%

evidence that these differences are driven by the sample preparation method, *i.e.*, the clusters have nucleated during ion milling.

The observations of a higher cluster number density and the nucleation of more Si-rich clusters can be explained by the clustering sequence after rapidly quenching an Al–Mg–Si alloy. When such an alloy is quenched from solution treatment temperatures, the Si atoms are the first to diffuse to the quenched-in vacancy clusters to stabilize them (Poznak et al., 2018) since Si has a positive binding energy and Mg has a negative binding energy to such vacancies (Wolverton, 2007; Wang et al., 2017). Therefore, the initial clusters that form at room temperature are Si-rich clusters, and over a period of few days of natural aging, Mg atoms will then segregate to the Si-vacancy stabilized clusters forming the observed Mg/Si co-clusters. Thus, the formation of Si-rich clusters is a distinct chemical signature of the newly formed clusters. The clear increase in Si-rich clusters in the PFIB sample and the balance of Si-rich and Mg-rich clusters in the FIB sample reveal that the ion milling has indeed facilitated an increase in the vacancy

concentration that enabled the Si in solution to now cluster by the introduction of vacancies created during milling. Furthermore, coupling the increase in Si-rich clusters with the higher total cluster density in the PFIB sample as compared to the FIB sample provides further evidence that the Xe$^+$ promoted a higher fraction of vacancy formation. Therefore, the number density and the chemical signature of these clusters (Si-rich versus Mg-rich) offer a direct means to measure how milling artificially evolved the nanostructure, even when the milling ions are not detected in the mass spectrum. This is further highlighted in the electropolished (PA + NA/30 days) sample in which the cluster characteristics are closer to the electropolished sample without any secondary natural aging. In the Famelton et al. (2021) report, where PFIB preparation was used, an increase in clusters was noted but attributed to a larger sampling volume. Additionally, average cluster compositions were provided. While the study concludes that PFIB results in minimal sample preparation artifacts, the above results strongly indicate otherwise. These results do suggest a checkpoint in the interpretation of APT data from PFIB-prepared samples, particularly for the early stages of cluster formation.

To understand the relative impact of Ga$^+$ and Xe$^+$ impingement on vacancy formation, SRIM modeling was performed (Ziegler et al., 2010). The Xe$^+$ and Ga$^+$ were implanted perpendicular to a pure Al surface with the vacancy profiles in Al for the Xe and Ga implantation plotted in Figure 3. Although Ga implantation results in vacancy formation at greater depth, Xe-based implantation results in a much higher surface vacancy concentration at a depth of up to 30 nm at 30 kV. This results in a large concentration of Xe-induced vacancies, some of which diffuse out of the needle to the free surface and are annihilated (Dumitraschkewitz et al., 2019). Nonetheless, it is likely that a
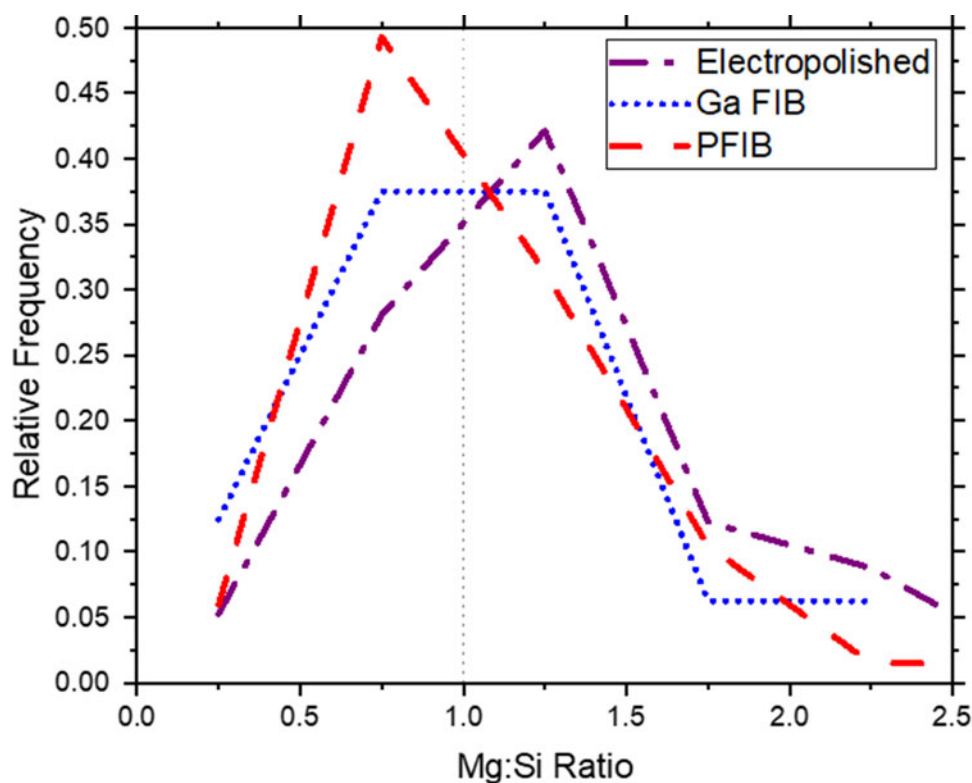
Fig. 2. Relative frequency histogram of the Mg:Si ratio of the clusters detected in the electropolished-, Ga$^+$ FIB-, and Xe$^+$ PFIB-prepared Al–Mg–Si samples.
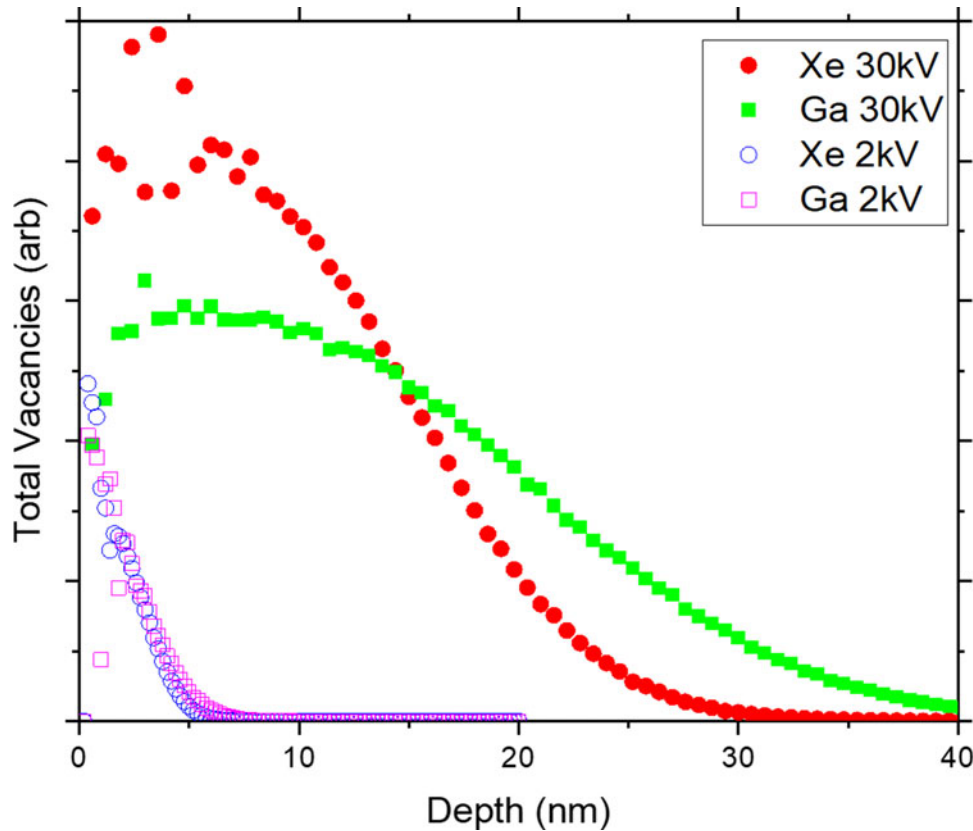
Fig. 3. SRIM calculated vacancy profiles for Ga and Xe implantation at 30 and 2 kV in Al.

significant number of these vacancies will become stabilized by the dissolved solute Si atoms in the alloy forming the observed Si-rich clusters discussed above. This process of clustering is extremely fast and occurs within 15 s at 0°C to stabilize such vacancy clustering (Ozawa & Kimura, 1970). This finding is critical because it demonstrates that Xe⁺ PFIB-prepared samples can indeed generate artificially higher cluster number densities in Al alloys. Although 2 kV polishing was used to minimize the FIB and PFIB-related damage, SRIM modeling indicates that vacancies are still induced up to 5 nm into the surface. For the Ga⁺ FIB-prepared sample, the significant concentration of Ga found throughout the sample (≈1.3 at%) indicates severe implantation which likely contributed to amorphization of the surface (consistent with large amounts of Ga at the surface, see inset image in Fig. 1e) and that existing clusters being annihilated under implantation explains the modest increase in the cluster density as compared to the electropolished sample.

Conclusion

This work reveals, quantitively, the substantial impact that ion milling can have on the solute clustering quantification in aluminum alloys using APT. Through a series of controlled experiments, the chemical signature of Si-rich clustering, as well as the increase in cluster density, provides supporting evidence that this ion milling creates new vacancies through implantation and knock-on events. Unlike Ga⁺ FIB milling, where the ion species is captured in the APT reconstruction providing direct chemical signature evidence of potential artifacts, the Xe⁺ PFIB ions were absent in its APT reconstruction. While this ion signature is not present, the PFIB milling has a higher deleterious artifact impact to the changes in the clustering nanostructure. Specifically, an increase in cluster density as compared to preparation where electropolishing or FIB milling is used results in the increase in vacancy density created by the Xe⁺. As Xe⁺ PFIB becomes an increasingly used as a tool in preparing Al alloys, these noted artifacts should be considered with any quantitative analysis and conclusion of the nanostructure, particularly with respect to the early stages of clustering.

References

Aruga Y, Kozuka M, Takaki Y & Sato T (2015). Formation and reversion of clusters during natural aging and subsequent artificial aging in an Al-Mg-Si alloy. *Mater Sci Eng A* **631**, 86–96.

Breen AJ, Moody MP, Ceguerra Av, Gault B, Araullo-Peters VJ & Ringer SP (2015). Restoring the lattice of Si-based atom probe reconstructions for enhanced information on dopant positioning. *Ultramicroscopy* **159**, 314–323.

Buchanan K, Colas K, Ribis J, Lopez A & Garnier J (2017). Analysis of the metastable precipitates in peak-hardness aged Al-Mg-Si(-Cu) alloys with differing Si contents. *Acta Mater* **132**, 209–221.

Buha J, Lumley RN, Crosky AG & Hono K (2007). Secondary precipitation in an Al-Mg-Si-Cu alloy. *Acta Mater* **55**, 3015–3024.

Dumitraschkewitz P, Gerstl SSA, Uggowitzer PJ, Löffler JF & Pogatscher S (2017). Atom probe tomography study of As-quenched Al–Mg–Si alloys. *Adv Eng Mater* **19**, 1–5.

Dumitraschkewitz P, Uggowitzer PJ, Gerstl SSA, Löffler JF & Pogatscher S (2019). Size-dependent diffusion controls natural aging in aluminium alloys. *Nat Commun* **10**, 1–6.

Famelton JR, Hughes GM, Williams CA, Barbatti C, Moody MP & Bagot PAJ (2021). Xenon plasma focussed ion beam preparation of an Al-6XXX alloy sample for atom probe tomography including analysis of an α-Al(Fe, Mn)Si dispersoid. *Mater Charact* **178**, 1–12.

Halpin JE, Webster RWH, Gardner H, Moody MP, Bagot PAJ & MacLaren DA (2019). An in-situ approach for preparing atom probe tomography specimens by xenon plasma-focussed ion beam. *Ultramicroscopy* **202**, 121–127.

Hu R, Liu J, Zhang Y & Sha G (2020). Revealing solute clusters in coalescence by atom probe tomography analysis. *Microsc Microanal* **26**, 1079–1087.

Hyde JM, Marquis EA, Wilford KB & Williams TJ (2011). A sensitivity analysis of the maximum separation method for the characterisation of solute clusters. *Ultramicroscopy* **111**, 440–447.

Idrissi H, Turner S, Mitsuhara M, Wang B, Hata S, Coulombier M, Raskin J, Pardoen T, Van Tendeloo G & Schryvers D (2011). Point defect clusters and dislocations in FIB irradiated nanocrystalline aluminium films: An electron tomography and aberration-corrected high-resolution ADF-STEM study. *Microsc Microanal* **17**, 983–990.

Jenkins BM, Douglas JO, Almirall N, Riddle N, Bagot PAJ, Hyde JM, Odette GR & Moody MP (2020). The effect of composition variations on the response of steels subjected to high fluence neutron irradiation. *Materialia* **11**, 1–11.

Kelley RD, Song K, Van Leer B, Wall D & Kwakman L (2013). Xe+ FIB milling and measurement of amorphous silicon damage. *Microsc Microanal* **19**, 862–863.

Larson DJ, Foord DT, Petford-long AK, Blamire MG, Cerezo A & Smith GDW (1999). Field-ion specimen preparation using focused ion-beam milling. *Ultramicroscopy* **79**(1–4), 287–293.

Larson DJ, Prosa TJ, Ulfig RM, Geiser BP, Kelly TF & Humphreys CJ (2013). *Local Electrode Atom Probe Tomography a User's Guide*. New York, Springer.

Lee SH, Jung JG, Baik Si, Seidman DN, Kim MS, Lee YK & Euh K (2021). Precipitation strengthening in naturally aged Al–Zn–Mg–Cu alloy. *Mater Sci Eng A* **803**, 1–8.

Lilensten L & Gault B (2020). New approach for FIB-preparation of atom probe specimens for aluminum alloys. *PLoS ONE* **15**, 1–9.

Marceau RKW (2016). Atomic scale analysis of light alloys using atom probe tomography. *Mater Sci Technol* **32**, 209–219.

Marquis EA & Hyde JM (2010). Applications of atom-probe tomography to the characterisation of solute behaviours. *Mater Sci Eng R Rep* **69**, 37–62.

Miller MK, Russell KF, Thompson K, Alvis R & Larson DJ (2007). Review of atom probe FIB-based specimen preparation methods. *Microsc Microanal* **13**, 428–436.

Ozawa E & Kimura H (1970). Excess vacancies and the nucleation of precipitates in aluminum-silicon alloys. *Acta Metall* **18**, 995–1004.

Poznak A, Marceau RKW & Sanders PG (2018). Composition dependent thermal stability and evolution of solute clusters in Al-Mg-Si analyzed using atom probe tomography. *Mater Sci Eng A* **721**, 47–60.

Stephenson LT, Moody MP, Gault B & Ringer SP (2013). Nearest neighbour diagnostic statistics on the accuracy of APT solute cluster characterisation. *Philos Mag* **93**, 975–989.

Thompson K, Gorman B, Larson D, van leer B & Hong L (2006). Minimization of Ga induced FIB damage using low energy clean-up. *Microsc Microanal* **12**(S02), 1736–1737.

Unocic KA, Mills MJ & Daehn GS (2010). Effect of gallium focused ion beam milling on preparation of aluminium thin foils. *J Microsc* **240**, 227–238.

Wang SS, Jiang JT, Fan GH, Panindre AM, Frankel GS & Zhen L (2017). Accelerated precipitation and growth of phases in an Al-Zn-Mg-Cu alloy processed by surface abrasion. *Acta Mater* **131**, 233–245.

Wolverton C (2007). Solute-vacancy binding in aluminum. *Acta Mater* **55**, 5867–5872.

Yao N & Zhong LW (2005). *Handbook of Microscopy for Nanotechnology*. New York, Kluwer Academic Publishers.

Ziegler JF, Ziegler MD & Biersack JP (2010). SRIM—The stopping and range of ions in matter. *Nucl Instrum Methods Phys Res B* **268**, 1818–1823.